



OPEN

Topologization of β -antimonene on Bi_2Se_3 via proximity effects

K. Holtgrewe¹, S. K. Mahatha^{2,3✉}, P. M. Sheverdyaeva², P. Moras², R. Flammini⁴, S. Colonna⁴, F. Ronci⁴, M. Papagno⁵, A. Barla², L. Petaccia⁶, Z. S. Aliev⁷, M. B. Babanly⁸, E. V. Chulkov^{9,10,11,12}, S. Sanna¹, C. Hogan⁴ & C. Carbone²

Topological surface states usually emerge at the boundary between a topological and a conventional insulator. Their precise physical character and spatial localization depend on the complex interplay between the chemical, structural and electronic properties of the two insulators in contact. Using a lattice-matched heterointerface of single and double bilayers of β -antimonene and bismuth selenide, we perform a comprehensive experimental and theoretical study of the chiral surface states by means of microscopy and spectroscopic measurements complemented by first-principles calculations. We demonstrate that, although β -antimonene is a trivial insulator in its free-standing form, it inherits the unique symmetry-protected spin texture from the substrate via a proximity effect that induces outward migration of the topological state. This “topologization” of β -antimonene is found to be driven by the hybridization of the bands from either side of the interface.

Ever since the discovery of the importance of topology in condensed matter physics¹, it has been demonstrated that the assembly of materials having different band structure topologies² gives rise to a plethora of novel physical phenomena. The transformation of a topological insulator (TI) into a superconductor^{3–5}, ferromagnetic TI⁶, or the appearance of Majorana fermions have been predicted³ and reported⁷. Topology has been invoked to explain the adsorbate/substrate resulting ferromagnetism^{8–10}. Even graphene, in contact with a TI, shows effects related to spin–orbit coupling (SOC)^{11,12}. These phenomena have been recognized as manifestations of a general “topological proximity effect”.

A conventional insulator (CI) and a TI, although sharing similar electronic structure in the bulk, at their interface feature a gap closing due to the different topological invariants². This process typically occurs via the emergence of metallic topological surface states (TSS), when spatially moving from the CI to the TI. In this paper we have investigated the behavior of the TSS that generally arise at the interface between the two insulators. The localization of the TSS can undergo a shift from the TI to the first layers of the CI, it may stay put at the interface, or it can move back inside the TI¹³. In other words, if a TSS migration arises at the interface, it can be the result of a “topologization” of the CI or a “trivialization” of the TI^{9,14–19}.

Gap size, SOC strength, work function difference, and relative thickness²⁰ of the CI and TI layers contribute to determine the properties of the resulting interface, as they drive the hybridization among atomic orbitals at the two sides of the interface. Structural aspects are also important: huge changes in the electronic structure have been predicted^{21,22} and experimentally reported as being due to lattice strain and to the relative orientation of the two lattices²³. A step forward has been made in the case of β -antimonene (i.e. the buckled honeycomb 2D allotrope of Sb) grown on bismuth selenide, where a perfect match at the interface is obtained with single orientation and negligible strain^{24–26}. A single, buckled β -antimonene sheet will be hereafter referred to as a bilayer (BL).

¹Institut für Theoretische Physik and Center for Materials Research (LaMa), Justus-Liebig-Universität Gießen, Heinrich-Buff-Ring 16, 35392 Gießen, Germany. ²Istituto di Struttura Della Materia, Consiglio Nazionale Delle Ricerche, 34149 Trieste, Italy. ³Ruprecht Haensel Laboratory, Deutsches Elektronen-Synchrotron DESY, 22607 Hamburg, Germany. ⁴Istituto di Struttura Della Materia, Consiglio Nazionale Delle Ricerche, Via del Fosso del Cavaliere 100, 00133 Roma, Italy. ⁵Dipartimento di Fisica, CS, Università Della Calabria, Via P. Bucci, 87036 Arcavacata di Rende, Italy. ⁶Elettra Sincrotrone Trieste, Strada Statale 14 km 163.5, 34149 Trieste, Italy. ⁷Azerbaijan State Oil and Industry University, AZ1010 Baku, Azerbaijan. ⁸Institute Catalysis and Inorganic Chemistry, Azerbaijan National Academy of Science, AZ1143 Baku, Azerbaijan. ⁹Departamento de Física de Materiales, UPV/EHU, 20080 Donostia-San Sebastian, Basque Country, Spain. ¹⁰Donostia International Physics Center (DIPC), P. de Manuel Lardizabal 4, 20018 San Sebastián, Basque Country, Spain. ¹¹Saint Petersburg State University, 198504 Saint Petersburg, Russia. ¹²Institute of Strength Physics and Materials Science, Russian Academy of Sciences, 634021 Tomsk, Russia. ✉email: sanjoymahatha@gmail.com

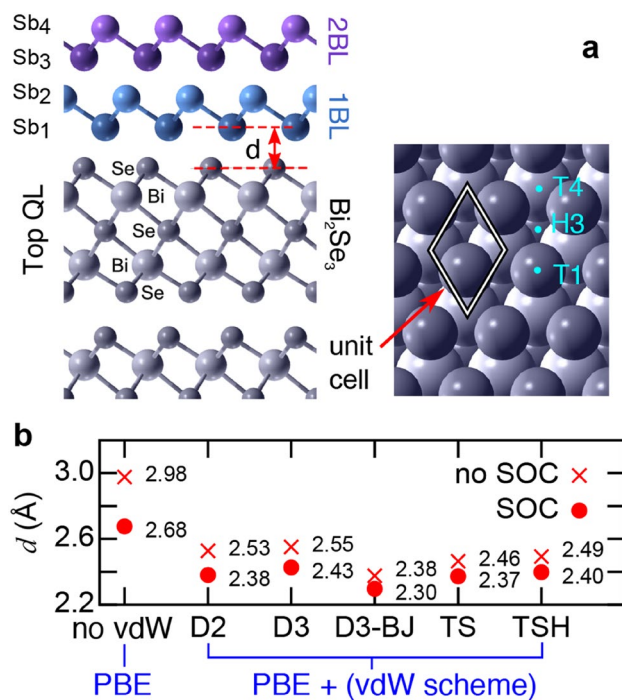


Figure 1. Structural properties of the β -antimonene/ Bi_2Se_3 hetero-junction. (a) Schematic structure of the β -antimonene/ Bi_2Se_3 interface for different coverages. The surface unit cell and interlayer spacing d are indicated, as well as positions of the T1 (atop Se), H3 (hollow), and T4 (atop Bi) sites. In the 1 BL case, the Sb_1 atom is adsorbed over the T4 (H3) site. The 2 BL layer follows the bulk stacking order, so that Sb_3 lies in the 1 BL hollow site. (b) Dependence of d for the 1 BL case on the vdW implementation (see text for details) and SOC.

The β -antimonene/ Bi_2Se_3 hetero-structure constitutes an archetypal system for studying these phenomena. Experimental evidence of a TSS migration has only been explicitly reported at the Bi/TI interface^{27,28} where the authors agree on the “topologization” of the bismuthene (i.e. honeycomb-like Bi) overlayer. However, one bilayer (BL) bismuthene hosts one-dimensional (1D) edge states^{29,30} typical of the quantum spin Hall phase (QSH), so that when deposited on top of a topological insulator, both 1D and 2D edge/surface states spatially coexist²⁷. In contrast, 1 BL and 2 BL of β -antimonene are trivial insulators³¹ while showing an important SOC as in the case of bismuth. This results in a simpler electronic structure, whose spin texture can be understood by atomistic calculations. This is of paramount importance in applications exploiting the electron spin, as tailoring the CI/TI spin textures can boost the realization of spintronics devices.

In the following we report on the atomic and electronic structures of atomically ordered β -antimonene layers on Bi_2Se_3 (0001). These systems have been examined by scanning tunneling microscopy and spectroscopy (STM/STS), angle-resolved photoemission spectroscopy (ARPES) and ab initio calculations within the density functional theory (DFT). STM images reveal the formation of ordered single and double BL of β -antimonene on Bi_2Se_3 , while STS of the unoccupied states reveal fingerprints of emergent topological bands. In both systems, ARPES measurements display well-defined dispersing bands, in good agreement with the calculated band structures. Hybridization between β -antimonene and Bi_2Se_3 determines the spin pattern of surface and interface electronic states. The formation of Dirac-cone surface-features demonstrates the topological character that β -antimonene inherits from the substrate via the proximity effect.

Results and discussion

The main issue with van der Waals (vdW) hetero-structures, is the difficulty in isolating a *single* overlayer phase in order to unambiguously characterize its electronic structure. Antimonene grown on Bi_2Se_3 forms at least two different allotropes: a puckered rectangular (α) and a buckled hexagonal (β) phase. We demonstrated a novel procedure for synthesizing large areas of lattice-matched β -antimonene on Bi_2Se_3 by means of a controlled structural transition from the α to the β phase^{25,26}. This results in a perfectly matched and oriented β -antimonene single phase on Bi_2Se_3 .

The resulting hetero-junction is shown in Fig. 1a. Each β -antimonene BL is composed of two Sb planes (Sb_1 and Sb_2 for the BL in contact with the substrate, Sb_3 and Sb_4 for the outer BL) arranged to form a buckled honeycomb structure. For the 1 BL case, we tested the influence of various vdW treatments on the DFT-calculated inter-layer spacing d , between β -Sb and Bi_2Se_3 , and report the results in Fig. 1b. The inclusion of any vdW treatment leads to consistently smaller values of d with respect to a pure PBE calculation. As a result, calculations neglecting vdW in determining the hetero-structure geometry may underestimate wave-function hybridization

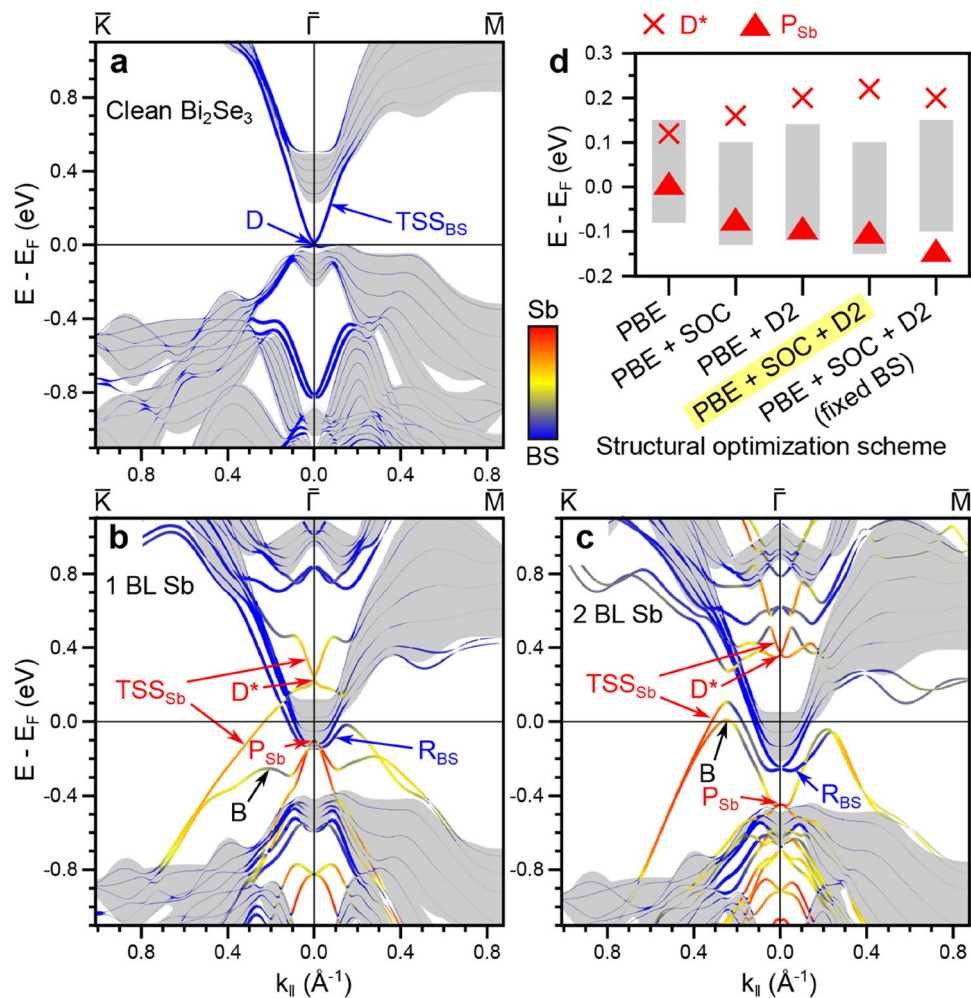


Figure 2. Computed band structures. (a) Bi_2Se_3 , (b) 1 BL and (c) 2 BL of β -antimonene on Bi_2Se_3 along $\bar{K} - \bar{\Gamma} - \bar{M}$ at the PBE-SOC-D2 geometry. The blue-to-red color gradient indicates the relative projection onto the BS front surface and Sb layers, respectively. Solid grey areas are the projected bulk bands. **d** Energy position at $\bar{\Gamma}$ of TSS_{Sb} (crosses) and P_{Sb} (triangles) for the 1 BL case using slab geometries computed with different schemes. The grey columns indicate the projected bulk conduction band at $\bar{\Gamma}$.

and lead to strong misalignments of β -antimonene and Bi_2Se_3 bands. Figure 1b also demonstrates the importance of accounting for SOC when computing the geometry. SOC reduces the inter-layer spacing d and has thus a similar effect as the vdW term. Since the semi-empirical D2 method³² yields results in good agreement with heavier *ab-initio* vdW flavours, and correctly describes the bulk Bi_2Se_3 geometry, we adopt henceforth the PBE + SOC + D2 geometries.

Band structures of clean Bi_2Se_3 , and with 1BL and 2BL of β -antimonene are reported in Fig. 2a–c along the $\bar{K} - \bar{\Gamma} - \bar{M}$ symmetry lines. The color scale of the bands indicates their spatial origin by means of projection onto atomic orbitals of (red) β -antimonene or (blue) Bi_2Se_3 surface (defined here as half the 6 QL slab). This allows to distinguish truly surface-localized states of Bi_2Se_3 from bulk states (projected bulk in gray). Orange/yellow lines indicate hybridized states of mixed β -antimonene/ Bi_2Se_3 (Sb/BS) character. The Fermi level (E_F) for both β -antimonene systems cuts the projected conduction band of bulk Bi_2Se_3 , in contrast to the case of clean Bi_2Se_3 , whose E_F is pinned at the Dirac point D of the topological surface state (TSS_{BS}). This reflects a charge transfer from Sb to the substrate upon deposition. Similar calculations have been reported previously for 1 BL¹⁴ and 2 BL of β -antimonene²⁴ on Bi_2Se_3 . We refer the reader to these works for a more detailed discussion of the origin of the band dispersion changes. Some important quantitative differences with respect to our calculations are discussed below.

Several bands are visible within the projected bulk gap. For the clean surface (Fig. 2a), the dominant feature is TSS_{BS} . The hetero-structures have more complicated band structures showing several hybridized bands for the single and double BLs. A topological surface state TSS_{Sb} with corresponding Dirac point D^* is evident in both systems. This state has a mixed orbital character for 1 BL and is of almost pure Sb-character near $\bar{\Gamma}$ in the 2 BL system (in fact it is localized more strongly on the outermost Sb bilayer). The hybridization with Sb leads to modifications of the band dispersion around D^* . For the 2 BL case, the effect of hybridization is so strong

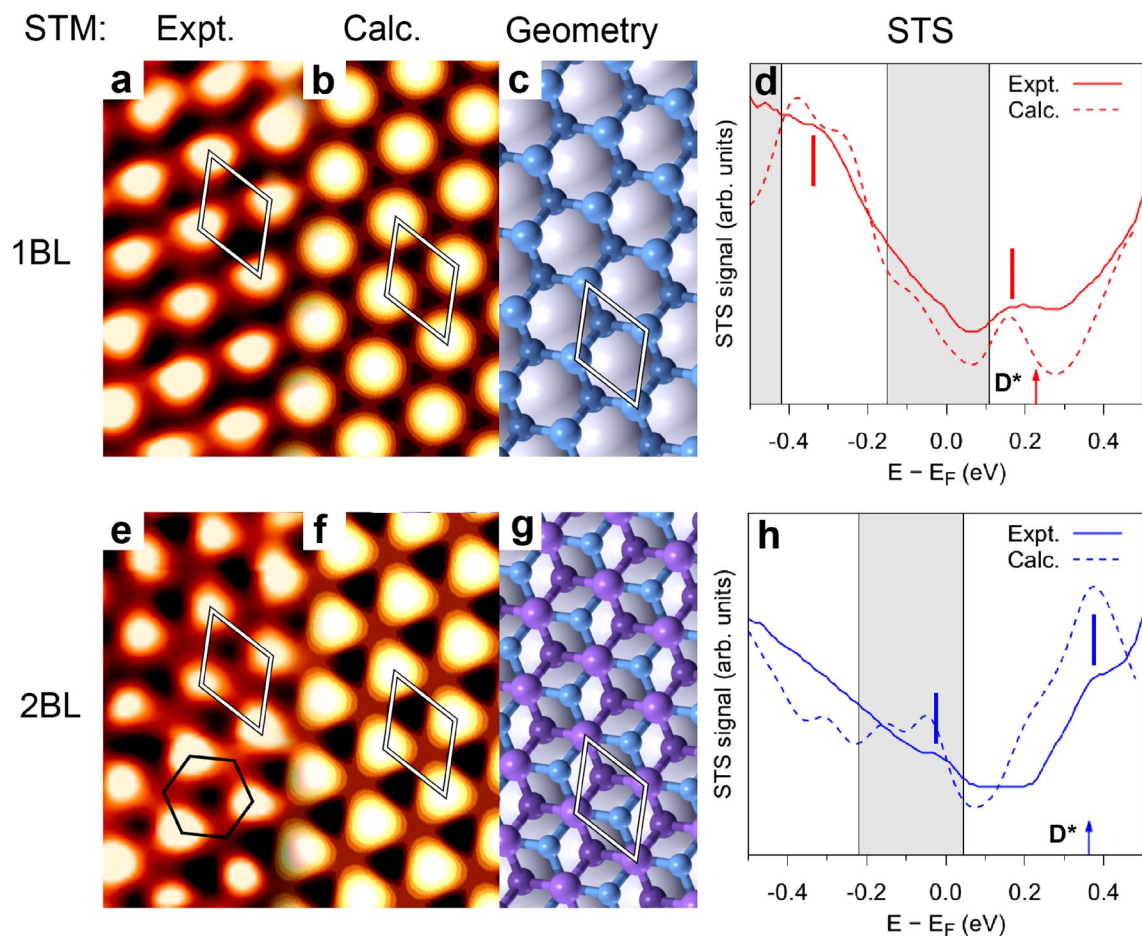


Figure 3. STM and STS measurements compared with theoretical calculations. The top and bottom rows refer to 1 BL and 2 BL β -antimonene/ Bi_2Se_3 , respectively. (a,e) $1.1 \times 2.2 \text{ nm}^2$ experimental STM images ($V_{\text{bias}} = +0.2 \text{ V}$, $I = 20 \text{ nA}$) and (b,f) simulated STM images ($V_{\text{bias}} = +0.2 \text{ V}$) based on the optimized structure shown in (c,g). (d,h) Experimental normalized $(dI/dV)/(I/V)$ STS spectra and computed LDOS. Grey regions indicate extent of projected bulk bands at $\bar{\Gamma}$ point; D^* indicates the calculated position of the emergent Dirac point in each case. Vertical bars represent the main experimental features (see text for discussion).

that the lower branch of the Dirac cone is unrecognizable. In both cases D^* appears in the projected bulk local gap above E_p , while the TSS_{Sb} are clearly distinguished within the absolute gap, below E_p . A dispersing band B of mixed orbital character is found below TSS_{Sb} and merges with it at larger wave-vector (k_{\parallel}) values for both Sb coverages. A state of almost pure Sb character (P_{Sb}) is found near the Bi_2Se_3 conduction band minimum for the 1 BL case, where also Rashba-split bands (R_{BS}), mainly deriving from the substrate, appear beside and below the bulk conduction bands. Similar Rashba bands are obtained for the 2 BL case, while P_{Sb} is shifted near the valence band maximum.

Previous calculations of the 1 BL structure placed D^* inside the Bi_2Se_3 conduction band and the apex of P_{Sb} inside the bulk gap¹⁴. We attribute this difference mostly to the omission of vdW interactions when optimizing the hetero-structure geometry. Figure 2d indicates the energetic position of P_{Sb} and D^* at $\bar{\Gamma}$ for the 1 BL case, as a function of the computational scheme adopted during the geometry optimization. The grey shaded area indicates the projected bulk conduction band. In the case of pure PBE (no vdW treatment), both D^* and P_{Sb} lie inside this band. Both points shift in energy, however, if vdW and/or SOC are included during the relaxation. Fixing the substrate geometry to that of bulk Bi_2Se_3 causes a strong misalignment of these bands with respect to the bulk bands (rightmost column). This stresses the importance of structural relaxation, dispersion and SOC in studies of such topologically-hybridized hetero-structures. Further modifications of the band structures are expected when quasi-particle corrections^{33–35} are considered.

Figure 3 shows (a) the STM image, (b) its DFT simulation, (c) the ball and stick model (top view, unit cell is highlighted) and (d) the experimental and simulated STS spectra for 1 BL β -antimonene on Bi_2Se_3 . The experimental and simulated STM images are in very good agreement and clearly show a hexagonal pattern determined by the upper Sb atoms (Sb_2 in Fig. 1a). An equivalent comparison for the 2 BL case is reported in Fig. 3e–h. Although the buckled atomic structure of the topmost BL is almost identical to that of the 1 BL case²⁶, the STM image is quite different, suggesting an important LDOS contribution to the STM images. The image is dominated by bright spots associated with the topmost Sb atoms (Sb_4), but in this case a clear apparent buckled honeycomb

pattern is observed in both measured and computed STM images. Similar simulated images are obtained for different positions of E_F from -0.15 eV to $+0.15$ eV.

The simulated STM image in panel (f) reveals that the apparent buckling does not derive from the geometrical buckling of the topmost Sb BL. Indeed, the Sb atom (Sb_3) in the unit cell in Fig. 3g is imaged as a hollow in both the experimental and simulated STM images. From analysis of the integrated local density of states (LDOS), we find that TSS_{Sb} strongly contributes to the 1 BL and 2 BL STM images reported in Fig. 3a,e (this is particularly true for the 1 BL case). The apparent buckling observed in the 2 BL STM images is actually determined by the shape and decay profile of the TSS_{Sb} wave-function.

Figure 3d,h shows a comparison between the measured normalized differential conductance $dI/dV/(I/V)$ spectra for the β -antimonene layers and the computed LDOS. The grey shaded areas indicate the projected bulk bands at the $\bar{\Gamma}$ point. The main experimental features are reproduced in the computed curves, such as the peaks at about -0.32 eV and $+0.18$ eV in the 1 BL case and the shoulders at -0.02 eV and $+0.38$ eV in the 2 BL spectra. Also evident is a “gap” in the 2 BL spectrum from about 0.05 to 0.23 eV that reflects a well-resolved minimum in the calculated data. The computed 1 BL curve in Fig. 3d shows a minimum very close to the position of the calculated D^* (0.23 eV): the alignment is not perfect due to the imposed broadening and nearby presence of the peak at 0.15 eV. Accordingly, the relative experimental curve shows a clear dip at the same energy, similarly to Sb on copper³⁶. The calculated 2 BL STS curve does not show a minimum in correspondence of the D^* energy, since the LDOS is dominated by peaks of similar energy. A comparison with the computed band dispersions reveals that the four peaks and shoulders in the STS derive from key surface states of the β -antimonene/ Bi_2Se_3 heterostructures. The peaks at $+0.18$ eV (1 BL) and $+0.38$ eV (2 BL) are fingerprints of the emergent topological surface states TSS_{Sb} , which exhibit strong curvature or even flattening in the vicinity of D^* . These features lie inside a gap in the projected bulk band structure as shown in Fig. 2b,c. In Ref.²⁴ a sharp peak in the STS spectrum of 2BL β -antimonene/ Bi_2Se_3 at about 0.45 eV is attributed to a stationary point in the substrate conduction bands (their calculations place D^* at 0.28 eV). However, their peak is well consistent with the sharp feature found at $+0.38$ eV in our computed LDOS arising from TSS_{Sb} in the vicinity of D^* . This discrepancy may be due to the neglect of vdW interactions in Ref.²⁴. The shoulders at -0.32 eV (1 BL) and -0.02 eV (2 BL) derive from the B bands which reverse slope at around 0.25 \AA^{-1} on either side of the $\bar{\Gamma}$ point.

Figure 4 displays ARPES spectra of Bi_2Se_3 and β -antimonene/ Bi_2Se_3 for different Sb coverages along the $\bar{\Gamma} - \bar{K}$ direction. Clean Bi_2Se_3 (Fig. 4a) shows a pair of linearly dispersing surface states near E_F that are identified as TSS_{Sb} . D occurs at -0.34 eV, in line with the results summarized in Ref.³⁷. Other intense bulk and surface features of Bi_2Se_3 are observed at larger binding energies. With the formation of 1 BL and 2 BL β -antimonene, new features appear in the Bi_2Se_3 band gap, while the substrate bands are attenuated and shifted to lower energies by the above discussed charge transfer process. Figure 4b,c shows data corresponding to Sb coverages below (0.6 BL) and slightly above (1.1 BL) the completion of 1 BL, respectively. In both cases two dispersing bands are observed between E_F and -1 eV. They split upon approaching the zone center: one branch crosses E_F ; the other reverses its dispersion after reaching about -0.3 eV. Figure 4d shows ARPES spectra for a full 2 BL β -antimonene. The dispersion of the Sb-induced features becomes sharper with respect to the 1 BL. Similarly to the 1 BL case, two bands are degenerate far from $\bar{\Gamma}$. Close to the zone center, one band crosses E_F whereas the other one bends to deeper energy. Another feature characteristic of the 2 BL system, and weakly visible in Fig. 4c, is observed at $\bar{\Gamma}$ with a maximum at -1 eV.

ARPES measurements on systems comprising few BL antimonene are available in the literature. Lei et al.³⁸ investigated sub-BL coverage. In Ref.²⁴, the ARPES spectra reported for 2BL actually correspond to a mixture of islands of different heights. In all cases, the samples are grown at RT and exhibit the presence of several allotropic phases^{25,26}. The features described here can be considered as true ARPES reference spectra for a *single* β -antimonene phase for 1 BL and 2 BL at *full* coverage.

Figure 5 compares the experimental and calculated band structures of 1 BL and 2 BL on Bi_2Se_3 along $\bar{M} - \bar{\Gamma} - \bar{M}$ and $\bar{K} - \bar{\Gamma} - \bar{K}$. In spite of the lack of quasi-particle corrections, and allowing for some misalignment of E_F , the overall agreement is rather good for 1 BL (Fig. 5a–d). The upper branch derives from the lower part of the TSS_{Sb} band, while the lower branch can be identified with the band B. Both bands have a hybrid Sb/ Bi_2Se_3 character. The Sb-related state P_{Sb} with maximum at -0.10 eV at $\bar{\Gamma}$ cannot be clearly distinguished in the experiment, however. This can be attributed to the overlap with the substrate conduction band and to matrix element effects: according to DFT, the state has purely p_x, p_y character and thus a low cross section in the photoemission experiments with p-polarized light in off-normal incidence.

Bands with an apparently similar dispersion in the proximity of E_F were observed also for Sb layers grown on other TIs^{38,39} and attributed to 1 Sb BL of unknown structure. However, the slopes of the bands for Sb layers on Sb_2Te_3 and Bi_2Te_3 are very different from the ones reported here and hardly compatible with the theoretical prediction. Theory predicts similar group velocities near E_F for the TSS_{Sb} bands on Sb_2Te_3 ($1.4 \text{ eV} \times \text{\AA}$), Bi_2Te_3 ($1.7 \text{ eV} \times \text{\AA}$) and Bi_2Se_3 ($1.3 \text{ eV} \times \text{\AA}$) substrates¹⁴. The group velocities measured for the TSS_{Sb} bands in Ref.³⁹ were $3.1 \text{ eV} \times \text{\AA}$ on Sb_2Te_3 and $2.5 \text{ eV} \times \text{\AA}$ on Bi_2Te_3 , i.e. almost twice larger than expected. In our DFT calculations we find a group velocity of approximately $1.5 \text{ eV} \times \text{\AA}$, which is in perfect agreement with the one determined by the ARPES data in Fig. 5 ($1.6 \text{ eV} \times \text{\AA}$).

Figure 5e–h shows the comparison of experimental and calculated band structure of 2 BL β -antimonene on Bi_2Se_3 . The overall agreement is even better than for the 1 BL case. The larger splitting of the upper and lower branches along $\bar{K} - \bar{\Gamma} - \bar{K}$ than along $\bar{M} - \bar{\Gamma} - \bar{M}$ is well reproduced. Moreover, the E_F crossing of these bands is also consistent. Only one band crosses E_F along $\bar{K} - \bar{\Gamma} - \bar{K}$, while no crossing is seen along $\bar{M} - \bar{\Gamma} - \bar{M}$. From the orbital-projected band structure one can again identify the two strongly dispersive bands with the emergent TSS_{Sb} band and the mixed origin of the B band. Furthermore, the band crossing near -0.3 eV at $\bar{\Gamma}$ (also present albeit less well resolved in the 1BL spectra) can be clearly interpreted as due to Rashba-split bands. According to the calculations, these bands are generated by the interface with β -antimonene but localized in the topmost

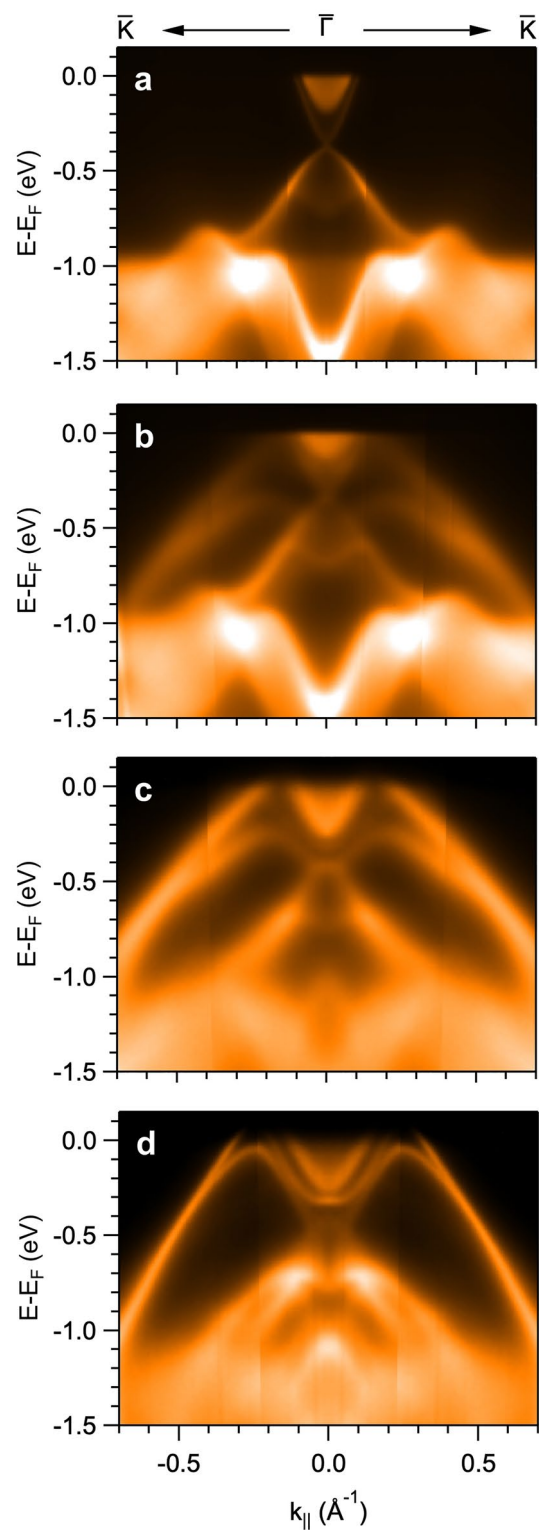


Figure 4. Experimental band structure. ARPES spectra measured with 20 eV photon energy along $\bar{K} - \bar{\Gamma} - \bar{K}$ of (a) Bi_2Se_3 , (b) 0.6 BL, (c) 1.1 BL and (d) 2 BL of β -antimonene/ Bi_2Se_3 .

Bi_2Se_3 QLs. Their orbital character is very different from that of the original TSS_{BS} , being derived from the bulk conduction band. The Rashba splitting is caused by local dipole moments between QLs associated with the charge transfer from the β -antimonene to the substrate^{40,41}.

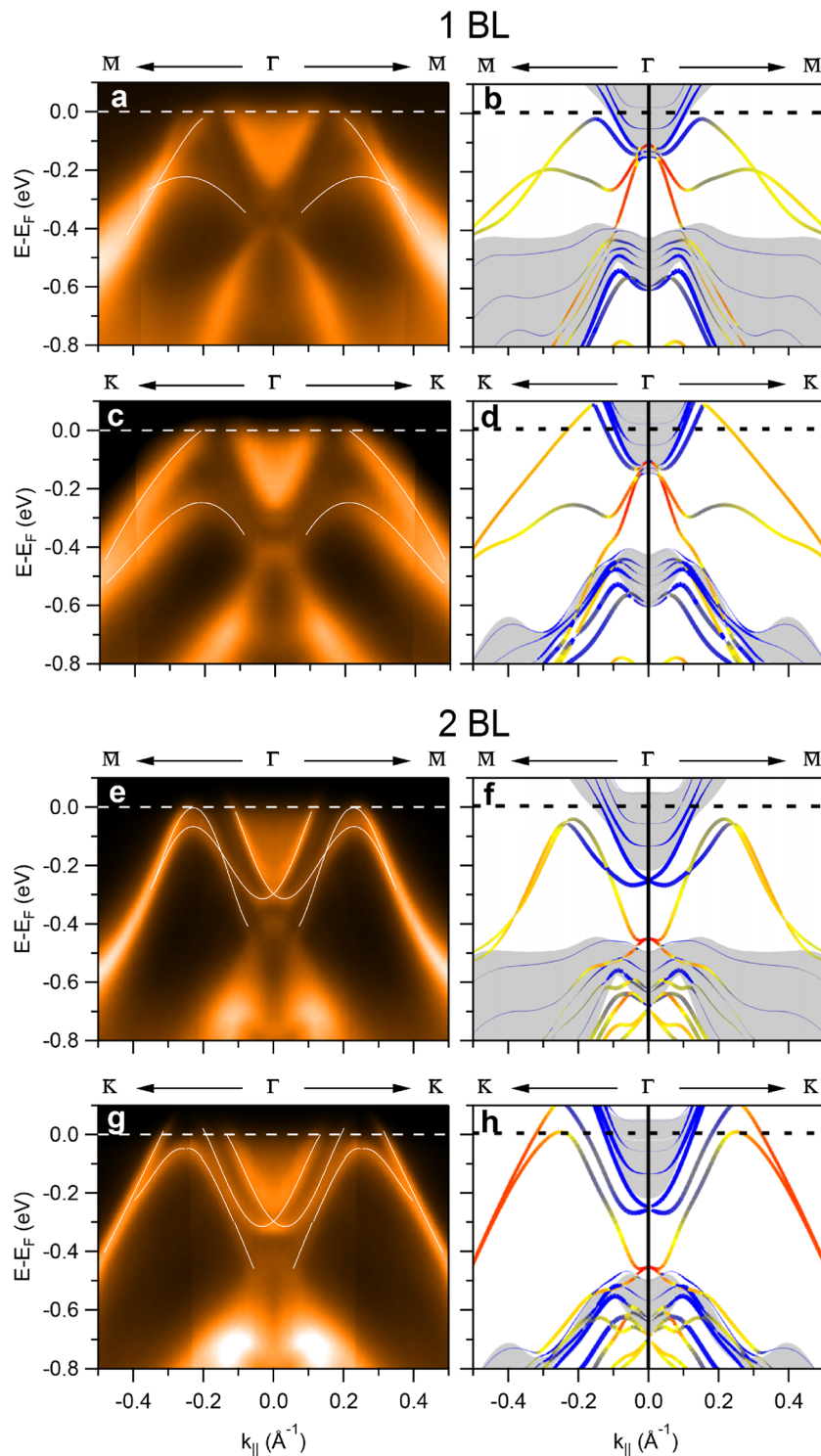


Figure 5. ARPES spectra and orbital-projected band structure. (a–d) 1 BL β -antimonene along the (first row) $\bar{M} - \bar{\Gamma} - \bar{M}$ and (second row) $\bar{K} - \bar{\Gamma} - \bar{K}$ directions. (e–h) Same as (a–d) for 2 BL β -antimonene.

We complete our analyses by considering the topological character of both systems as revealed by DFT. We verified that the free-standing 1 BL and 2 BL β -antimonene films are topologically trivial insulators by computing the Z_2 topological invariants (see Supplementary Information for details) following the parity method of Fu and Kane⁴². This finding is consistent with previous calculations that predict a trivial-topological crossover to a quantum spin Hall phase for layers of at least 4 BLs³¹. We also note that an odd number of bands cross the fundamental gap along $\bar{\Gamma} - \bar{M}$, in both cases due to the single TSS_b branch that connects the bulk valence band to the bulk conduction band^{2,43}.

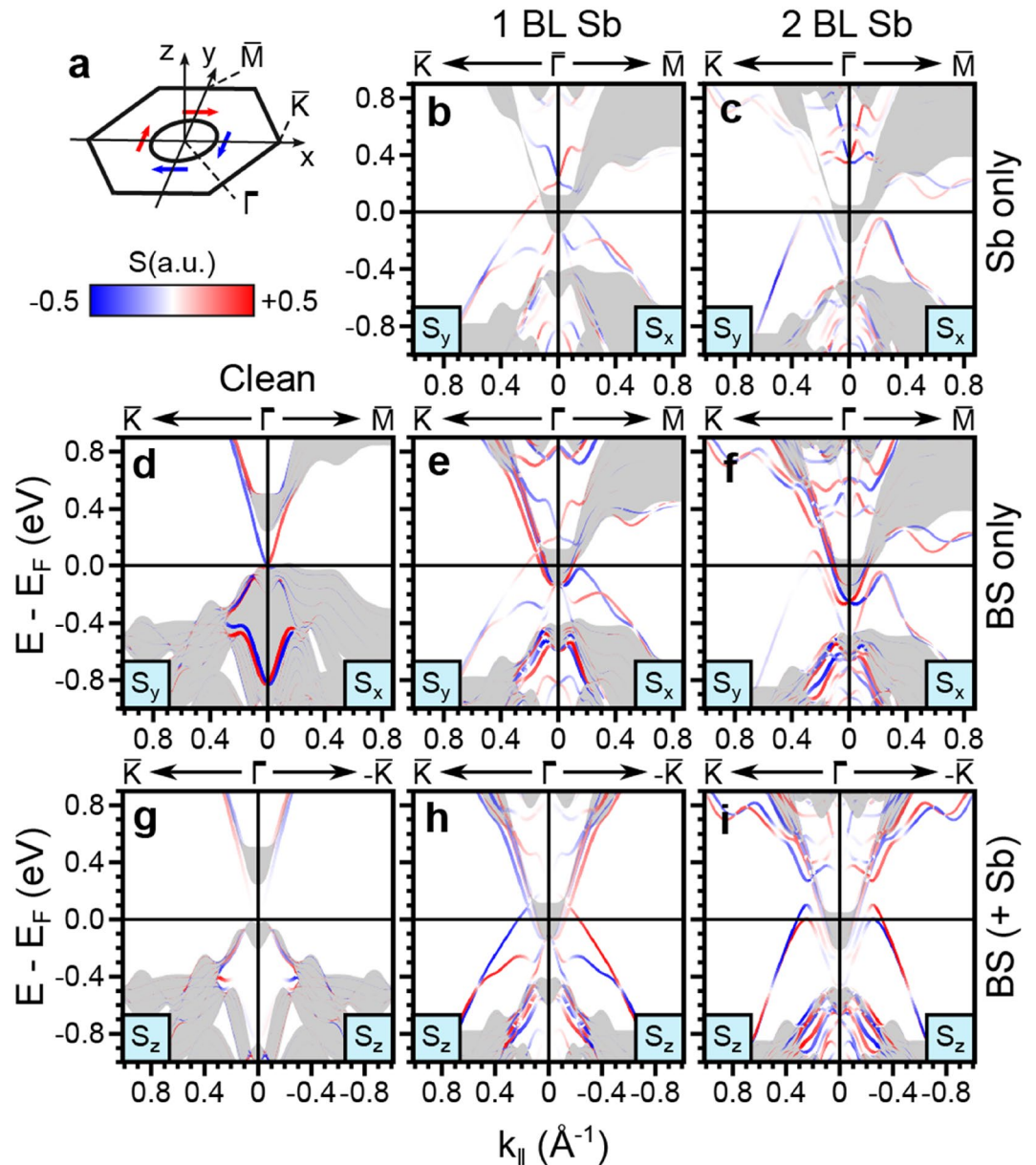


Figure 6. Computed spin texture. (a) Brillouin zone geometry. (b–i) Spin textures of Bi_2Se_3 (left column) and additional 1 BL β -antimonene (centre column) and 2 BL β -antimonene (right column). (b–f) In-plane S_x and S_y components projected on the β -antimonene layer (top row) and the top QL (middle row). (g–i) S_z component, for selected spatial projections. Spin up and spin down channels are represented in blue and red, respectively.

The calculated spin texture of the clean Bi_2Se_3 and β -antimonene/ Bi_2Se_3 hetero-structures is reported in Fig. 6. Figure 6b–f displays the S_x and S_y components of the spin expectation value along $\bar{K}-\bar{\Gamma}-\bar{M}$ (i.e. perpendicular to k_x and k_y , as defined in Fig. 6a), projected on the β -antimonene layers (top row) and topmost Bi_2Se_3 QL (middle row), respectively. Zero polarization is found along the direction parallel to k [See Fig. S3 and S4 of Supplementary Information]. Figure 6g–i shows the out-of-plane component of the spin expectation value S_z along $\bar{K}-\bar{\Gamma}-\bar{K}$. While S_z is practically zero in pure Bi_2Se_3 , it becomes strong for the hetero-structures, even close to the $\bar{\Gamma}$ point for some bands. This may derive from a hexagonal warping effect induced by the β -antimonene layer⁴⁴ or from considerable orbital momentum contributions⁴⁵. Several bands such as the band of mixed Sb/BS character labeled B, as well as TSS_{Sb} in the 1 BL case, show k dependent rotations in S_y . The B band in particular has a dominant S_z component. In contrast, the Rashba-like character of R_{BS} is confirmed by the spin texture which is completely confined to the substrate and lies fully within the surface plane (zero S_z component). The second band crossing lying in the projected local bulk gap was clearly detected in the experiment (see around -1.1 eV in Fig. 4d) which likely corresponds to the Rashba-split bands seen here at -0.8 eV in the calculation. These latter bands have strong Sb character and thus have $S_z=0$ only around the $\bar{\Gamma}$ point.

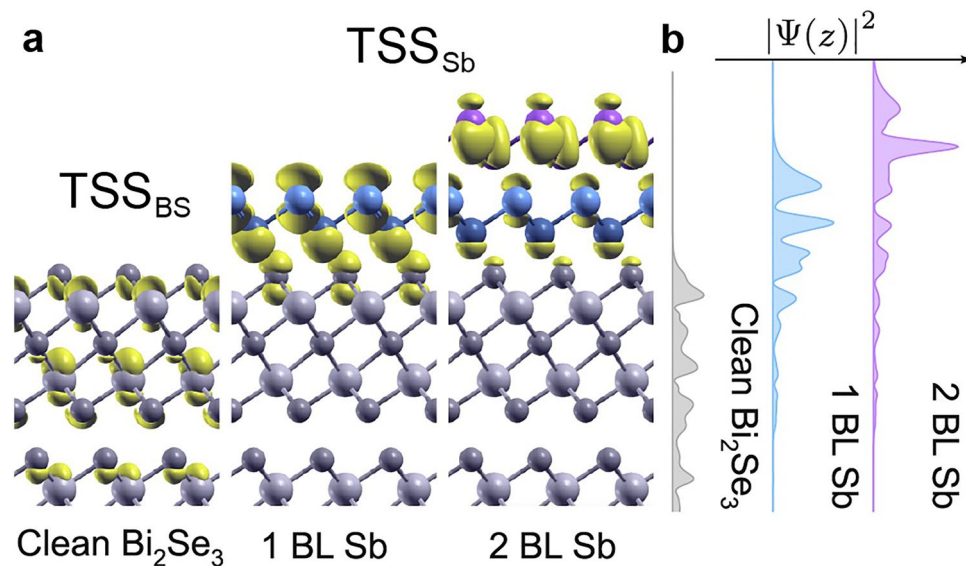


Figure 7. The real space character of TSS_{BS} and TSS_{Sb} . (a) Isosurfaces of TSS_{BS} or TSS_{Sb} at the $\bar{\Gamma}$ point and (b) their planar-averaged profiles.

Spin analysis along the $\bar{K}-\bar{\Gamma}-\bar{K}$ direction (see Figs. S3 and S4 of Supplementary Information) confirms the helical nature of TSS_{Sb} . The 1 BL bands show a similar spin pattern to that of the substrate, wherein the spin magnetization density axis is locked perpendicular to k . For the 2 BL case, the spin polarization of TSS_{Sb} within the surface plane shows the same spin-momentum locking, at least in a narrow range around $\bar{\Gamma}$ well above the E_F . The spin polarization of the TSS decreases from the center to the boundary of the Brillouin zone for the S_x and S_y , while the opposite occurs for the S_z . This is generally ascribed to the superposition with bulk projected states⁴⁶. TSS_{Sb} thus displays the character of an emergent topologically protected state. By the comparison of the spin texture around the D (clean Bi_2Se_3) and D^* points (either 1 BL or 2 BL), we note that the spin texture associated with the original TSS persists following hybridization with Sb states. In contrast, TSS_{BS} is barely present in the Sb-covered surfaces (being hidden by the bulk valence band), implying that the state has lost its character (and topological protection) upon interfacing of the Sb layer.

The spin texture of TSS_{Sb} derives mostly from the β -antimonene BL(s), although there is also a considerable contribution from the topmost QL in the 1 BL case, as expected from the orbital projection data (Fig. 2b,c). Figure 7a,b show TSS_{BS} and TSS_{Sb} in real space as isosurface plots of $|\Psi|^2$ at the $\bar{\Gamma}$ point and as plane-averaged plots, respectively. These plots at the D and D^* points demonstrate the change in the character and localization of the topological state as a function of the Sb coverage. All three states have a similar total extension perpendicular to the surface (10–15 Å). The TSS_{BS} state spans the whole topmost quintuple layer, as well as the first two atomic layers of the second QL, and derives from a mixture of Bi and Se orbitals. The TSS_{Sb} is distributed across and outside the β -antimonene in the 1 BL system, with some contribution from the substrate (especially Se p_z orbitals). Its depth profile is thus very similar to that of clean Bi_2Se_3 , although it has clearly shifted towards the β -antimonene layer. The depth profile for 2 BL TSS_{Sb} is quite different, being more strongly localized at the outermost β -antimonene BL and with weaker contributions from lower Sb and Se atoms. The different orbital origin of the two TSS_{Sb} states conclusively explains the differences between their STM images in Fig. 3. The associated bands and spin texture around the D and two D^* points (compare Fig. 6b,c,d) nonetheless remain strikingly similar.

These observations confirm that TSS_{Sb} and the Dirac point at D^* are truly emergent features and constitute a manifestation of a proximity effect in which an adsorbed trivial insulator (β -antimonene) inherits the unique electronic properties of a TI substrate (Bi_2Se_3). In other words, the helical state floats to the top of the CI (β -antimonene) which acquires a topological character⁴⁷. The hybridization with the substrate demonstrates that Bi_2Se_3 does not provide a platform for realizing free-standing β -antimonene, in spite of its vdW nature²⁶. However, it opens up the possibility to harness the topological nature of the Bi_2Se_3 substrate along with its momentum-locked spin character.

Conclusions

The preparation of large areas of single β -phase of antimonene on Bi_2Se_3 allowed to record unprecedentedly detailed ARPES and STM/STS reference spectra for 1BL and 2BL. Accurate quantum mechanical simulation including vdW and SOC have been performed to interpret the experimental data. The excellent agreement achieved with respect to the measured ARPES, STS, and STM data allows a consistent analysis of the experiments and provide a sound theoretical description of the underlying physical phenomena.

Our approach reveals a migration of TSS from the TI substrate to the outermost atomic layers of the CI. The migration occurs in a step-by-step manner as 1 and 2 BL of β -antimonene are adsorbed. In other words, the

particular electronic character of the β -antimonene/Bi₂Se₃ hetero-structures makes it possible to successfully *extract* the TSS from the TI surface and transfer it to the topmost atomic layers of the topologically trivial insulator. This behavior confirms the process of CI “topologization” in the hetero-structure, as distinct from the predicted “trivialization” of the TI in MnSe/Bi₂Se₃⁹, or the absence of migration of the TSS as predicted theoretically in ZnS/Bi₂Se₃¹³. The spatially extended character of TSS in β -antimonene/Bi₂Se₃ demonstrates that it originates from the topology of bulk Bi₂Se₃, although orbital analysis reveals that it acquires considerable Sb character due to increasing hybridization. This origin appears to differ from previous suggestions²⁴.

The TSS migration is facilitated by the perfect lattice match of β -antimonene/Bi₂Se₃. Other vdW hetero-structures with incommensurate interfaces, like a phase of antimonene on Bi₂Se₃²⁶, could hinder such migration due to the different interface potential, orbital hybridization, and local geometry, leading to topological states with different dispersion and localization. Lattice matching is therefore crucial in the design of vdW hetero-structures with topological properties.

From a technological point of view, the β -antimonene/Bi₂Se₃ heterostructures considered here do not directly offer a route towards dissipationless currents, as bulk conduction bands open multiple scattering channels at E_F . It might be feasible to tune the position of the D^* points into the bulk fundamental gap by means of surface doping⁴⁸ or external strain⁴⁹. Yet, the strong perturbation of the lower Dirac cones towards a Rashba-like character may offer alternative possibilities for probing electronic excitations of topologically protected helical states via inverse photoemission⁵⁰, two-photon photoemission^{51,52}, or optical techniques^{53,54}.

Finally, symmetry protection allows the migration of the TSS from a TI substrate to an adsorbate layer that is both elementally and structurally different. This includes the change in symmetry from the hexagonal Se layer to the honeycomb Sb, as well as the change from a passivated substrate to one with dangling bonds. This is relevant to all the cases where the surface of the TI is not suitable to an epitaxial growth or to a functionalization. Ultimately, this may open a novel route towards easier handling of materials made of TI interfaced with metal contacts for the next generation of devices.

Methods

Sample preparation, STM/STS and ARPES measurements. Antimony was sublimated in in-situ cleaved Bi₂Se₃ at RT with a deposition rate of 0.5 Å/min, followed by a prolonged annealing at 473 K²⁵. The Sb coverage calibration was based on the known structural properties of the Ag₂Sb surface alloy on Ag(111), which presents a $(\sqrt{3} \times \sqrt{3})R30^\circ$ reconstructed surface⁵⁵. The structural ordering of the sample was confirmed by low-energy electron diffraction (LEED). STM images were measured by using an Omicron LT-STM instrument operating at 80 K. An electrochemically etched W wire was used as STM tip after electron bombardment cleaning in UHV. The STM scanner was calibrated measuring the clean Bi₂Se₃(0001) surface. The bias voltage is referred to the sample, hence positive (negative) bias corresponds to empty (filled) states. STS measurements have been acquired at 80 K using a lock-in amplifier with gap modulation at 5 kHz and 10 mV peak-to-peak amplitude. The STS spectra were collected on a 30 × 30 nm² image on a grid of 80 × 80 points. The reported spectra were obtained by averaging the normalized differential conductance curves $(dI/dV)/(I/V)$ for 1 and 2 BL of β -antimonene. Photoemission experiments were performed at the VUV-Photoemission and BaDElPh⁵⁶ beamlines of Elettra (Trieste, Italy). ARPES measurements were conducted at 80 K, with an angular resolution better than 0.3° and energy resolution of 30 meV.

Calculation method. DFT calculations were performed using the Vienna ab initio simulation package (VASP)^{57,58}. Plane waves (kinetic energy cutoff of 400 eV) and projector augmented wave (PAW) pseudopotentials [(15 valence electrons for Bi (electronic configuration 5d¹⁰ 6s² 6p³), 6 valence electrons for Se (4s² 4p⁴), and 5 for Sb (5s² 5p³)] were used, yielding well-converged (to 1 meV/Å) geometries and total energies. A Γ -centered 12 × 12 × 1 k-point mesh was used. The Bi₂Se₃ substrate was described using a 6 QL centrosymmetric slab, separated from periodically repeating replicas by thick (> 50 Å) vacuum regions. The experimentally determined atomic positions⁵⁹ and lattice constants ($a = 4.143$ Å and $c = 28.636$ Å) were adopted. Sb atoms and the top four atomic layers of the substrate were allowed to relax. β -antimonene/Bi₂Se₃ hetero-structures were modelled by placing Sb atoms on both sides of the slab in their most stable geometries²⁵. The PBE exchange–correlation functional⁶⁰ was employed with a correction to account for dispersion/vdW forces. The vdW approaches considered include Grimme’s semi-empirical schemes: D2³⁵, D3 without damping⁶¹, and D3-BJ with Becke–Johnson damping⁶², as well as the approach of Tkatchenko–Scheffler (TS)⁶³ also with iterative Hirschfeld partitioning (TSH)⁶⁴. Note that for bulk Bi₂Se₃, PBE-SOC-D2 yields interlayer distances very close to the experimental one. STM images were simulated via constant local density of states (LDOS) isosurfaces corresponding to the Tersoff–Hamann approximation. STS spectra were obtained by integrating the LDOS inside a 1.5 Å-thick box placed 2.5 Å above the topmost surface atom, and applying a broadening of 0.04 eV.

Data availability

The data that support the findings of this study are available from the corresponding authors upon request.

Received: 17 June 2020; Accepted: 19 August 2020

Published online: 03 September 2020

References

1. See for example: Asorey, M. Space, matter and topology. *Nat. Phys.* **12**, 616–618 (2016).
2. Hasan, M. Z. & Kane, C. L. Colloquium: topological insulators. *Rev. Mod. Phys.* **82**, 3045–3067 (2010).

3. Fu, L. & Kane, C. L. Superconducting proximity effect and majorana fermions at the surface of a topological insulator. *Phys. Rev. Lett.* **100**, 096407 (2008).
4. Maier, L. *et al.* Induced superconductivity in the three-dimensional topological insulator HgTe. *Phys. Rev. Lett.* **109**, 186806 (2012).
5. Xu, J.-P. *et al.* Artificial topological superconductor by the proximity effect. *Phys. Rev. Lett.* **112**, 217001 (2014).
6. Wei, P. *et al.* Exchange-coupling-induced symmetry breaking in topological insulators. *Phys. Rev. Lett.* **110**, 186807 (2013).
7. Nadj-Perge, S. *et al.* Observation of majorana fermions in ferromagnetic atomic chains on a superconductor. *Science* **346**, 602–607 (2014).
8. Vobornik, I. *et al.* Magnetic proximity effect as a pathway to spintronic applications of topological insulators. *Nano Lett.* **11**, 4079 (2011).
9. Ereemeev, S. V., Men'shov, V. N., Tugushev, V. V., Echenique, P. M. & Chulkov, E. V. Magnetic proximity effect at the three-dimensional topological insulator/magnetic insulator interface. *Phys. Rev. B* **88**, 144430 (2013).
10. Hirahara, T. *et al.* Large-gap magnetic topological heterostructure formed by subsurface incorporation of a ferromagnetic layer. *Nano Lett.* **17**, 3493–3500 (2017).
11. Popov, I., Mantega, M., Narayan, A. & Sanvito, S. Proximity-induced topological state in graphene. *Phys. Rev. B* **90**, 035418 (2014).
12. Bian, G. *et al.* Experimental observation of two massless Dirac-fermion gases in graphene-topological insulator heterostructure. *2D Mater.* **3**, 021009 (2016).
13. Wu, G. F. *et al.* Tuning the vertical location of helical surface states in topological insulator heterostructures via dual-proximity. *Sci. Rep.* **3**, 1233 (2013).
14. Jin, K. H., Yeom, H. W. & Jhi, S. H. Band structure engineering of topological insulator heterojunctions. *Phys. Rev. B* **93**, 075308 (2016).
15. Hutasoit, J. A. & Stanescu, T. D. Induced spin texture in semiconductor/topological insulator heterostructures. *Phys. Rev. B* **84**, 085103 (2011).
16. Menshchikova, T. V. *et al.* Band structure engineering in topological insulator based heterostructures. *Nano Lett.* **13**, 6064–6069 (2013).
17. Essert, S., Krueckl, V. & Richter, K. Using topological insulator proximity to generate perfectly conducting channels in materials without topological protection. *New J. Phys.* **16**, 113058 (2014).
18. Seixas, L., West, D., Fazzio, A. & Zhang, S. B. Vertical twinning of the Dirac cone at the interface between topological insulators and semiconductors. *Nat. Commun.* **6**, 7630 (2015).
19. Men'shov, V. N., Tugushev, V. V., Ereemeev, S. V., Echenique, P. M. & Chulkov, E. V. Band bending driven evolution of the bound electron states at the interface between a three-dimensional topological insulator and a three-dimensional normal insulator. *Phys. Rev. B* **91**, 075307 (2015).
20. Costa, M. *et al.* Controlling topological states in topological/normal insulator heterostructures. *ACS Omega* **3**, 15900–15906 (2018).
21. Huang, Z. Q. *et al.* Strain driven topological phase transitions in atomically thin films of group IV and V elements in the honeycomb structures. *New J. Phys.* **16**, 105018 (2014).
22. Zhang, S., Yan, Z., Li, Y., Chen, Z. & Zeng, H. Atomically thin arsenene and antimonene: semimetal–semiconductor and indirect–direct band-gap transitions. *Angew. Chem. Int. Ed.* **54**, 3112–3115 (2015).
23. Markl, T. *et al.* Engineering multiple topological phases in nanoscale Van der Waals heterostructures: realisation of α -antimonene. *2D Mater.* **5**, 011002 (2018).
24. Kim, S. H. *et al.* Atomically abrupt topological p-n junction. *ACS Nano* **11**, 9671–9677 (2017).
25. Flammini, R. *et al.* Evidence of β -antimonene at the Sb/Bi₂Se₃ interface. *Nanotechnology* **29**, 065704 (2018).
26. Hogan, C. *et al.* Temperature driven phase transition at the antimonene/Bi₂Se₃ van der Waals heterostructure. *ACS Nano* **13**, 10481–10489 (2019).
27. Hirahara, T. *et al.* Interfacing 2D and 3D topological insulators: Bi(111) bilayer on Bi₂Te₃. *Phys. Rev. Lett.* **107**, 166801 (2011).
28. Shoman, T. *et al.* Topological proximity effect in a topological insulator hybrid. *Nat. Commun.* **6**, 6547 (2015).
29. Murakami, S. Quantum spin hall effect and enhanced magnetic response by spin-orbit coupling. *Phys. Rev. Lett.* **97**, 236805 (2006).
30. Wada, M., Murakami, S., Freimuth, F. & Bihlmayer, G. Localized edge states in two-dimensional topological insulators: ultrathin Bi films. *Phys. Rev. B* **83**, 121310 (2011).
31. Zhang, P., Liu, Z., Duan, W., Liu, F. & Wu, J. Topological and electronic transitions in a Sb(111) nanofilm: the Interplay between quantum confinement and surface effect. *Phys. Rev. B* **85**, 1410 (2012).
32. Grimme, S. Semiempirical GGA-type density functional constructed with a long-range dispersion correction. *J. Comput. Chem.* **27**, 1787–1799 (2006).
33. Nechaev, I. A. *et al.* Evidence for a direct band gap in the topological insulator Bi₂Se₃ from theory and experiment. *Phys. Rev. B* **87**, 121111 (2013).
34. Aguilera, I., Friedrich, C., Bihlmayer, G. & Blügel, S. GW study of topological insulators Bi₂Se₃, Bi₂Te₃, and Sb₂Te₃: beyond the perturbative one-shot approach. *Phys. Rev. B* **88**, 045206 (2013).
35. Förster, T., Krüger, P. & Rohlfing, M. Two-dimensional topological phases and electronic spectrum of Bi₂Se₃ thin films from GW calculations. *Phys. Rev. B* **92**, 201404 (2015).
36. Niu, T. *et al.* Modulating epitaxial atomic structure of antimonene through interface design. *Adv. Mater.* **31**, 1902606 (2019).
37. Frantzeskakis, E. *et al.* Trigger of the ubiquitous surface band bending in 3D topological insulators. *Phys. Rev. X* **7**, 041041 (2017).
38. Lei, T. *et al.* Anisotropic electronic structure of antimonene. *Appl. Phys. Lett.* **115**, 221602 (2019).
39. Lei, T. *et al.* Electronic structure of antimonene grown on Sb₂Te₃(111) and Bi₂Te₃ substrates. *J. Appl. Phys.* **119**, 015302 (2016).
40. Bahramy, M. S. *et al.* Emergent quantum confinement at topological insulator surfaces. *Nat. Commun.* **3**, 1159 (2012).
41. Förster, T., Krüger, P. & Rohlfing, M. Ab initio studies of adatom- and vacancy-induced band bending in Bi₂Se₃. *Phys. Rev. B* **91**, 035313 (2015).
42. Fu, L. & Kane, C. L. Topological insulators with inversion symmetry. *Phys. Rev. B* **76**, 045302 (2007).
43. Hsieh, D. *et al.* Observation of unconventional quantum spin textures in topological insulators. *Science* **323**, 919–922 (2009).
44. Fu, L. Hexagonal warping effects in the surface states of the topological insulator Bi₂Te₃. *Phys. Rev. Lett.* **103**, 266801 (2009).
45. Gotlieb, K. *et al.* Symmetry rules shaping spin-orbital textures in surface states. *Phys. Rev. B* **95**, 245142 (2017).
46. Takayama, A., Sato, T., Souma, S. & Takahashi, T. Rashba effect in antimony and bismuth studied by spin-resolved ARPES. *New J. Phys.* **16**, 055004 (2014).
47. Xiao-Guang, L. *et al.* Proximity effects in topological insulator heterostructures. *Chin. Phys. B* **22**, 097306 (2013).
48. Roy, S. *et al.* Tuning the dirac point position in Bi₂Se₃(0001) via surface carbon doping. *Phys. Rev. Lett.* **113**, 116802 (2014).
49. Liu, Y. *et al.* Tuning dirac states by strain in the topological insulator Bi₂Se₃. *Nat. Phys.* **10**, 294–299 (2014).
50. Datzler, C. *et al.* Unraveling the spin structure of unoccupied states in Bi₂Se₃. *Phys. Rev. B* **95**, 115401 (2017).
51. Reimann, J., Güdde, J., Kuroda, K., Chulkov, E. V. & Höfer, U. Spectroscopy and dynamics of unoccupied electronic states of the topological insulators Sb₂Te₃ and Sb₂Te₂S. *Phys. Rev. B* **90**, 081106 (2014).
52. Kung, H.-H. *et al.* Observation of chiral surface excitons in a topological insulator Bi₂Se₃. *Proc. Natl. Acad. Sci.* **116**, 4006–4011 (2019).
53. Sobota, J. A. *et al.* Direct optical coupling to an unoccupied dirac surface state in the topological insulator Bi₂Se₃. *Phys. Rev. Lett.* **111**, 136802 (2013).
54. Panna, D. *et al.* Linear-optical access to topological insulator surface states. *Appl. Phys. Lett.* **110**, 212103 (2017).

55. Noakes, T. C., Hutt, D. A., McConville, C. F. & Woodruff, D. P. Structural investigation of ordered Sb adsorption phases on Ag(111) using coaxial impact collision ion scattering spectroscopy. *Surf. Sci.* **372**, 117–131 (1997).
56. Petaccia, L. *et al.* BaDElPh: A 4m normal-incidence monochromator beamline at Elettra. *Nucl. Instrum. Methods Phys. Res. Sect. A* **606**, 780–784 (2009).
57. Kresse, G. & Furthmüller, J. Efficiency of ab-initio total energy calculations for metals and semiconductors using a plane-wave basis set. *Comput. Mater. Sci.* **6**, 15–50 (1996).
58. Kresse, G. & Furthmüller, J. Efficient iterative schemes for ab initio total-energy calculations using a plane-wave basis set. *Phys. Rev. B* **54**, 11169 (1996).
59. Nakajima, S. The crystal structure of $\text{Bi}_2\text{Te}_{3-x}\text{Se}_x$. *J. Phys. Chem. Solids* **24**, 479 (1963).
60. Perdew, J. P., Burke, K. & Ernzerhof, M. Generalized gradient approximation made simple. *Phys. Rev. Lett.* **77**, 3865–3868 (1996).
61. Grimme, S., Antony, J., Ehrlich, S. & Krieg, H. A consistent and accurate ab initio parametrization of density functional dispersion correction (DFT-D) for the 94 elements H–Pu. *J. Chem. Phys.* **132**, 154104 (2010).
62. Grimme, S., Ehrlich, S. & Goerigk, L. Effect of the damping function in dispersion corrected density functional theory. *J. Comput. Chem.* **32**, 1456–1465 (2011).
63. Tkatchenko, A. & Scheffler, M. Accurate molecular van der Waals interactions from ground-state electron density and free atom reference data. *Phys. Rev. Lett.* **102**, 073005 (2009).
64. Bucko, T., Lebègue, S., Hafner, J. & Ángyán, J. G. Improved density dependent correction for the description of London dispersion forces. *J. Chem. Theory. Comput.* **9**, 4293 (2013).

Acknowledgements

Calculations were performed at the Hazel Hen cluster at the Höchstleistungsrechenzentrum Stuttgart (HLRS), the Lichtenberg cluster at TU Darmstadt, the Center for Materials Research at JLU Gießen, and the CINECA Supercomputing Centre at Bologna. The authors acknowledge the computational resources and support provided by the HPC Core Facility and the HRZ of the Justus-Liebig Universität, and by CINECA via the ISCRA initiative. Technical support from Giovanni Emma, Massimiliano Rinaldi, Luca Sancin, and Fabio Zuccaro is acknowledged. We acknowledge the project EUROFEL-ROADMAP ESFRI. E.V.C. acknowledges support from the Saint Petersburg State University (Grant No. 51126254) and Fundamental Research Program of State Academies of Sciences for 2019–2021 (research direction III.23.2.9). The authors wish to thank Elettra Sincrotrone Trieste for providing access to its synchrotron radiation facilities.

Author contributions

S.K.M. and C.C. conceived the project. K.H. and C.H. performed the calculations and analysis with support from S.S. and E.V.C. S.K.M., P.M.S., P.M., R.F., A.B., M.P., L.P., and C.C. performed the ARPES measurements and analyses. F.R., S.C., and R.F. performed the S.T.M. and S.T.S. measurements and analysis. Z.S.A. and M.B.B. prepared the substrate. The manuscript was written by S.K.M., R.F., S.S., C.H., and C.C. and contributed to by all authors.

Funding

Open Access funding provided by Projekt DEAL.

Competing interests

The authors declare no competing interests.

Additional information

Supplementary information is available for this paper at <https://doi.org/10.1038/s41598-020-71624-4>.

Correspondence and requests for materials should be addressed to S.K.M.

Reprints and permissions information is available at www.nature.com/reprints.

Publisher's note Springer Nature remains neutral with regard to jurisdictional claims in published maps and institutional affiliations.



Open Access This article is licensed under a Creative Commons Attribution 4.0 International License, which permits use, sharing, adaptation, distribution and reproduction in any medium or format, as long as you give appropriate credit to the original author(s) and the source, provide a link to the Creative Commons licence, and indicate if changes were made. The images or other third party material in this article are included in the article's Creative Commons licence, unless indicated otherwise in a credit line to the material. If material is not included in the article's Creative Commons licence and your intended use is not permitted by statutory regulation or exceeds the permitted use, you will need to obtain permission directly from the copyright holder. To view a copy of this licence, visit <http://creativecommons.org/licenses/by/4.0/>.

© The Author(s) 2020